

# Fluid Lubricated Dexterous Finger Mechanism for Human-Like Impact Absorbing Capability

Yong-Jae Kim<sup>✉</sup>, Member, IEEE, Junsuk Yoon, and Young-Woo Sim<sup>✉</sup>

**Abstract**—This letter presents a novel three degree-of-freedom finger mechanism that features excellent impact absorbing performance, high force, and precision comparable to human hands. Inspired by human fingers, it has a simple structure with a minimum number of rigid components: seven rigid frames, several polymer wires, and flexible sheets. For impact absorption, rolling contact joints with a center ligament, instead of conventional revolute joints with bearings or bushings, were used. While this mechanism can be dislocated in the event of off-axis bending or twisting force and impact, it can return afterward without degrading precision. To achieve precise manipulation performance, a unique tendon guiding structure, which enables accurate kinematic modeling even though it is composed of soft and flexible materials, is proposed. To prevent loss of precision and robustness against friction, the whole mechanism is covered by an artificial skin and filled with lubrication liquid, which is similar to human synovial fluid. The developed finger mechanism can exert 40 N fingertip force in a straight pose and has 0.2 mm repeatability of fingertip position under multiple impacts. Various experiments including button clicking and wheel rotation of a computer mouse demonstrated the performance and potential usefulness of the proposed mechanism.

**Index Terms**—Bioinspired mechanism, compliant mechanism, flexible robots, robotic hand, tendon-driven mechanism.

## I. INTRODUCTION

**H**UMAN hands are known to be one of the most versatile body mechanisms having a high level of performance. They can precisely manipulate small objects, even to the scale of submillimeter, and also lift an entire human body. One of their most impressive properties is their robustness against impact and overload. Such remarkable performance is achieved by

Manuscript received February 23, 2019; accepted June 30, 2019. Date of publication July 22, 2019; date of current version August 2, 2019. This letter was recommended for publication by Associate Editor K. Yamane and Editor P. Rocco upon evaluation of the reviewers' comments. This work was supported by the convergence technology development program for bionic arm through the National Research Foundation of Korea (NRF) funded by the Ministry of Science & ICT NRF-2015M3C1B2052817. (Corresponding author: Yong-Jae Kim.)

Y.-J. Kim and J. Yoon are with the Department of Electronic Engineering, Korea University of Technology and Education, Cheonan-City 31253, South Korea (e-mail: yongjae@koreatech.ac.kr; ynkbo401@koreatech.ac.kr).

Y.-W. Sim is with the Department of Mechanical and Aerospace Engineering, Seoul National University, Seoul-City 08826, South Korea (e-mail: ywsim@snu.ac.kr).

This letter has supplementary downloadable material available at <http://ieeexplore.ieee.org>, provided by the authors. This video introduces a novel three degree-of-freedom finger mechanism that features excellent impact absorbing performance, high payload, and precision comparable to human hands. This MPEG-4 video is known to be compatible with Microsoft Media Player or other players. Contact (yongjae@koreatech.ac.kr) for further questions about this letter.

Digital Object Identifier 10.1109/LRA.2019.2929988

the combination of just four rigid bones per finger with soft tissues, including six tendons for actuation. Such performance is, however, hard to achieve in robotic hands made of precisely machined strong frames and conventional components. The anatomy of a human hand shows its elaborate and delicate structure, but its anatomical features alone cannot explain its remarkable characteristics.

Researchers have sought to understand the operation of human hands, and to exploit this in designing a robotic mechanism [1], [2]. ACT Hand is a well-known robotic hand developed to understand the intrinsic biomechanical and control features in human hands [1]. Using these mechanisms, the relationship between the actuating tendons and hand postures was clearly identified and the dexterity of the proposed mechanism was verified. However, the design of these devices did not seek to replicate the high strength and robustness of human hands.

In human hands, the large extrinsic muscles for power grasp, the flexor digitorum profundus (FDP) and the flexor digitorum superficialis (FDS), are located in the forearm. The tensions of these muscles are transmitted to the fingers through the tendons named FDP tendon and FDS tendon. This remote actuation is also beneficial for robotic hands because the size of the hand can be reduced without sacrificing strength. Many robotic hands [3], [4] including the one reported in the author's previous work [5] utilize this approach. Using tendons for remote actuation may create substantial friction. The mechanisms to avoid this can be complicated and require difficult fabrication and expensive components. To lower mechanical complexity, hands with reduced degrees-of-freedom (DOF) using under-actuated mechanisms or utilizing synergy [6], [7], [10], [11] are also being actively researched. However, there are still many innovations that need to be achieved for robotic hand capabilities to be comparable to those of humans. To deal with external impact, various types of series elastic actuators (SEA) or variable stiffness joints (VSJ) have been developed and applied [3].

To accomplish human-like dexterity and strength, as well as robustness to impact, this letter introduces a novel cable-driven finger mechanism that is not based on conventional components and structures. Fig. 1 shows the proposed mechanism, named FLLEX Finger (FLuid Lubricated dEXterous finger), together with the anatomy of the human finger. FLLEX Finger has been developed with considerable inspiration from the biomechanical properties of human hands. However, instead of mimicking the shape of the human anatomy, the principles of the performance of human hands were adopted but with a thorough understanding of the differences of materials and fabrication between organisms and artificial mechanisms. Materials include rigid frames made from acrylonitrile butadiene styrene (ABS), several polymer wires for actuation and joint constraining, and flexible sheets for wire guiding. The proposed rolling contact joints, with a center

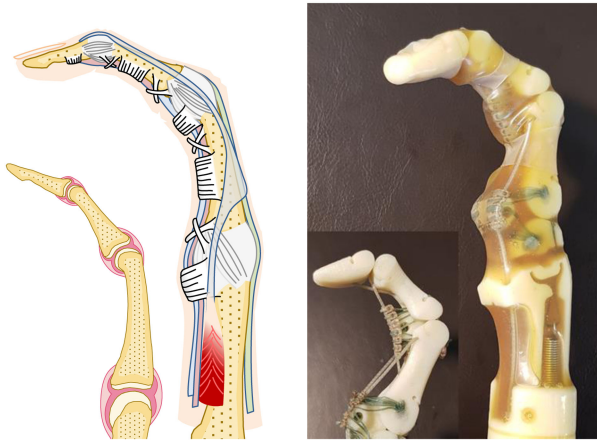


Fig. 1. Proposed FLLEX finger (FLuid Lubricated dEXterous finger), (right side) with the anatomy of the human finger (left side).

ligament, can endure high compressive force while being able to be dislocated in the event of an off-axis force and impact, and it can return afterwards without ill-effects on precision. A unique tendon guiding structure enables accurate kinematic modeling even though it is composed of soft and flexible materials. To minimize friction, the whole mechanism is covered by an artificial skin and filled with a liquid suitable for lubrication of polymer materials.

The remainder of this letter is organized as follows. Section II describes the properties of human hands from an engineering point of view and compares this with robotic hands. In Section III, the design philosophy and the mechanical design are presented. In Section IV, the kinematics and statics of the finger mechanism are described. Section V presents the experimental design and reports the evaluation results, and Section VI provides some concluding remarks.

## II. COMPARISON OF HUMAN AND ROBOTIC HANDS

As illustrated in Fig. 2(a), each human finger, except the thumb, has four phalangeal bones: metacarpal, proximal, intermediate, and distal phalanges. The 3 joints, named the metacarpophalangeal (MCP), the proximal interphalangeal (PIP), and the distal interphalangeal (DIP) joint, have 2, 1, and 1 DOFs, respectively. The synovial membranes surround the joints and fill them with synovial fluid, which provides protection and lubrication between the two cartilages. One hand is composed of 27 bones, including eight carpal bones, and has 23 DOFs actuated by more than 30 muscles.

Each joint is constrained by multiple ligaments including collateral ligaments and volar ligaments as shown in Fig. 2(b). These ligaments prevent hyperextension and sideways bending of the joints. In addition, the tensions of the collateral ligaments enable a joint to return to a neutral pose when the actuating tendons are relaxed. Moreover, with the help of ligaments, the human joints can comply with a certain level of excessive force and impact instead of being destroyed while resisting it. As illustrated in Fig. 2(b), six muscles are connected to the phalangeal bones via tendons, where three intrinsic muscles are simplified to one muscle. Among these, the two tendons FDP and FDS provide large flexion force when gripping and pinching. Interestingly, all the tendons and muscles are also enclosed by synovial sheaths and filled with the synovial fluid, which dramatically reduces the friction even when tendon paths are

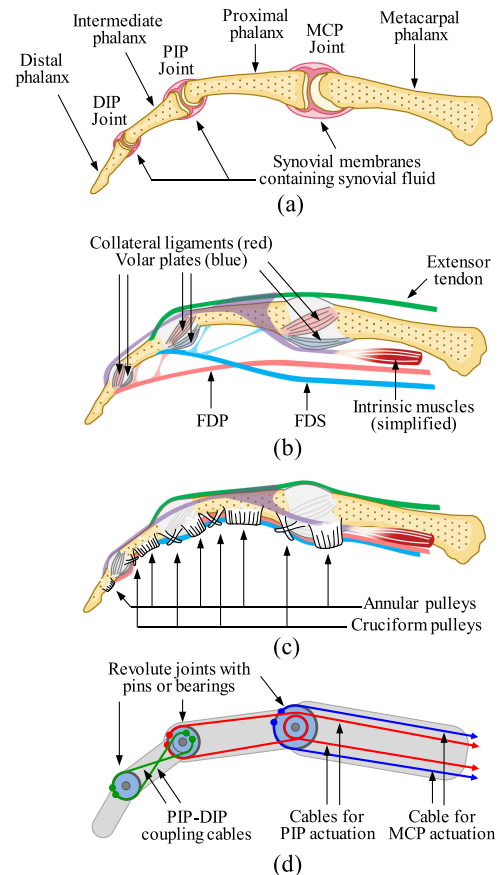


Fig. 2. Anatomy of human fingers: (a) phalanges and joints surrounded by synovial membranes. (b) and (c) simplified illustration of the ligaments, tendons, muscles, and pulleys. (d) example of a cable-driven robotic finger.

largely bent. For instance, the measured friction coefficient of the human shoulder joint is 0.0015 [8], which is smaller than the frictional coefficient of ball bearings. The pulleys in the human hand shown in Fig. 2(c), which are also a kind of ligament, form a tunnel on the palmar aspect of the hand through which the FDP and FDS pass. Due to these pulleys, and the volar ligaments with protruding joint shape, the tendons can maintain the proper moment arm from the joint.

Fig. 2(d) shows a simplified model of a cable-driven robot finger. To achieve the joint motion without slack, two antagonistic cables are attached to a circular pulley on each joint. The exactly antagonistic motion of the cable pairs enables precise motion with a relatively simple actuation mechanism, but the small moment arm, the result of the small radius of the circular pulley, hinders increase of joint torque. Moreover, the complex cable route can make the mechanism complicated and cause friction, especially when the abduction/adduction motion of the MCP joint is also implemented (omitted in Fig. 2(d)). For instance, RoboRay Hand [5], a five-fingered 14-DOF robotic hand, is composed of 400 machined parts of aluminum alloy and steel. In addition, to accomplish high precision with low friction, 242 miniature ball bearings were used. Such mechanisms based on these conventional components are vulnerable to impact or excessive force because the bearings and bushings get damaged by a force exceeding the maximum load. Excessive force to the joint bending direction within the range of motions can be absorbed by using impact-absorbing actuators such as back-drivable actuators, SEAs or VSJ [3]. However, off-axis

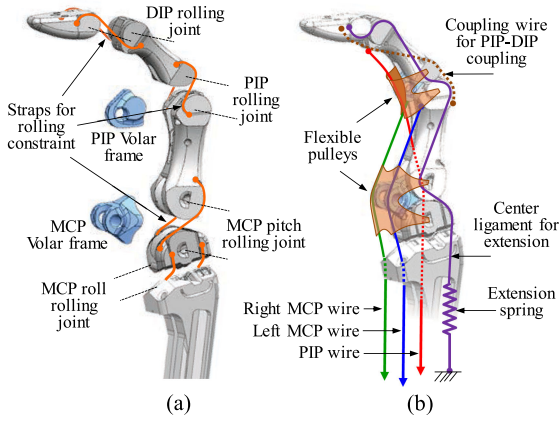


Fig. 3. Mechanical design of the FLLEX finger. (a) Rigid frames and the coupling wires. (b) Actuation wires and flexible pulleys.

forces and hyperextensions that exceed the range of motion can cause serious damage.

The maximum fingertip force of an adult index finger is higher than 40 N, which is also challenging for human-size high-DOF robotic hands, even though they have stronger frames and cables than human bones and tendons. This performance of human hands is thought to originate from the optimal structure of the tendon, pulleys, and phalanges, which provide a large moment arm and efficient tension routing. The FLLEX finger was developed considering the principles responsible for this outstanding human hand performance. The design philosophy of the FLLEX finger is as follows:

- 1) Robustness against impact and overload using compliant structures without decreasing strength and precision.
- 2) High force similar to human hands by efficient tendon routings and a large moment arm.
- 3) Kinematically accurate mechanisms for precise manipulation, where the kinematics is exactly defined even though soft and flexible materials are utilized.
- 4) Simple mechanism minimizing the number of rigid components, using easily accessible materials such as 3D-printing materials, polymer wires, and laser-cut fabrics.

### III. MECHANICAL DESIGN OF THE FLLEX HAND

As shown in Fig. 3(a), the proposed 3-DOF finger mechanism has seven 3-D printed rigid frames. The length from the MCP roll rolling joint to the fingertip is 110 mm, similar to human fingers. All the joints are rolling contact joints and, to allow pure rolling motion, one side of each rolling contact joint is constrained by a pair of non-stretchable straps (orange curves). The rolling joint has less friction than bushings and higher allowable compressive force than bearings. For instance, miniature ball bearings have point contacts between the balls and bearing races, but the rolling joint has line contact between two cylinders with large radius. Thus, it can withstand higher compressive force. The other side of each rolling contact joint is constrained by one wire named the center ligament (purple curve in Fig. 3(b)), which is connected by an extension spring and provides passive extension torques to all the PIP, DIP and MCP pitch joints. This center ligament with the extension spring allows off-axis motion without damage when the joint receives excessive force. Utilizing passive extension simplifies the mechanism and is thus frequently used,

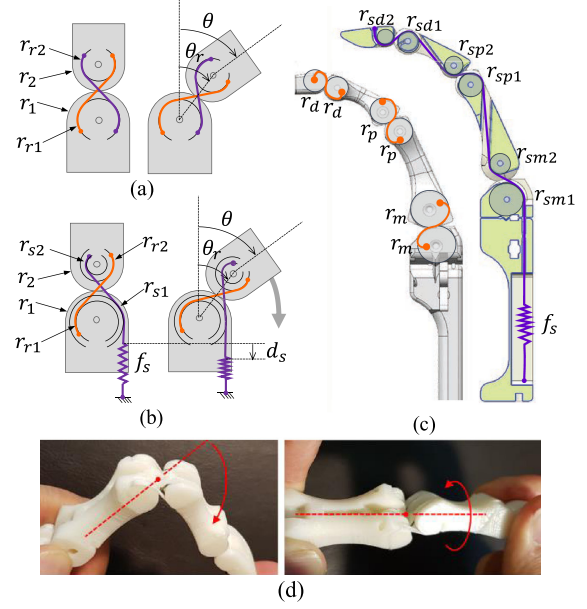


Fig. 4. Impact absorbing link structure with a center ligament, (a) conventional rolling joint. (b) Proposed rolling joint producing extension torque. (c) and (d) design and implementation of the proposed link structure.

as in [6], [7]. However, it can limit the extension torque, and an improperly selected passive extension torque could cause loss of grasping force or vibration during arm motion. The PIP and MCP volar frames, shown in Fig. 3(a), are inserted at the PIP and MCP pitch joints to secure sufficient moment arm between the frame and the actuation wires. The red curve in Fig. 3(b), named PIP wire, produces the flexion motion of the PIP joint. The blue and green wires in Fig. 3(b), named left MCP and right MCP wires respectively, produce the MCP flexion motion and MCP ab/adduction motion.

The two flexible pulleys in Fig. 3(b) maintain the PIP and MCP wires in the proper route, thereby avoiding bowstring effects. The PIP-DIP coupling wire (brown dotted curve) couples the two joint angles to have a constant ratio of 3:2.

#### A. Impact Absorbing Link Structure With a Center Ligament

To endure high compressive force, as well as to comply with excessive off-axis bending and twisting, a unique link mechanism based on rolling joints which produce extension torques is proposed. Fig. 4(a) shows a conventional rolling joint mechanism, where  $r_1$  and  $r_2$  are the radii of the rolling contact surfaces which need not be the same. For pure rolling without slip, the coupling wires can be used as marked by the orange and purple curves in the figure. To maintain constant tension, the radii of the circular surfaces for the two coupling wires,  $r_{r1}$  and  $r_{r2}$ , should have the same ratio of  $r_1$  and  $r_2$ , that is

$$\frac{r_1}{r_2} = \frac{r_{r1}}{r_{r2}} \quad (1)$$

When the bending angle is  $\theta$ , the angle of the line between the centers of the rolling surfaces  $\theta_r$  can be easily calculated, as shown in the right figure of Fig. 4(a) as

$$\theta_r = \frac{r_2}{r_1 + r_2} \theta \quad (2)$$



If we set a different ratio between  $r_1/r_2$  and  $r_{r1}/r_{r2}$  in (1) intentionally, joint torque can be produced. In Fig. 4(b), one of the coupling wires (purple curve) has a different radii ratio, where  $r_{s1}$  and  $r_{s2}$  denote the changed radii. The proximal end of the coupling wire is tensioned by a constant force  $f_s$  produced by a constant force spring. If the joint rotates to angle  $\theta$ , the coupling wire around the lower circular part is released and the wire around the upper circular part is further wound. Thus, the change in the total length of the coupling wire  $d_s$  can be obtained as follows:

$$d_s = \theta_r r_{s1} - (\theta - \theta_r) r_{s2}$$

Substituting  $\theta_r$  into this with (2),

$$d_s = \frac{r_2 r_{s1} - r_1 r_{s2}}{r_1 + r_2} \theta \quad (3)$$

This implies that if the ratio of  $r_{s1}$  and  $r_{s2}$  is the same as that of  $r_1$  and  $r_2$ , in other words, if it satisfies (1), the length change  $d_s$  becomes zero. Otherwise, the length change produces bending torque. Considering the conservation of virtual work ( $f_s d_s = \tau_s \theta$ ), the produced torque  $\tau_s$  can be calculated as follows:

$$\tau_s = \frac{r_2 r_{s1} - r_1 r_{s2}}{r_1 + r_2} f_s \quad (4)$$

Fig. 4(c), illustrates the DIP, PIP, and MCP rolling joints and the route of the center ligament. In our implementation, the rolling surface and the surfaces for the coupling wires with a fixed length of each joint were set to have the same radii ( $r_1 = r_2 = r_{r1} = r_{r2}$  in (4)), and the radii for the center ligament were selected to produce proper extension torques as follows:

$$\begin{aligned} \tau_{s\_MCP} &= \frac{r_{sm1} - r_{sm2}}{2} f_s, \\ \tau_{s\_PIP} &= \frac{r_{sp1} - r_{sp2}}{2} f_s, \\ \tau_{s\_DIP} &= \frac{r_{sd1} - r_{sd2}}{2} f_s \end{aligned} \quad (5)$$

where  $\tau_{s\_MCP}$ ,  $\tau_{s\_PIP}$ , and  $\tau_{s\_DIP}$  denote the extension torques of the MCP pitch, PIP, and DIP joints, respectively, and  $r_{sm1}$ ,  $r_{sm2}$ ,  $r_{sp1}$ ,  $r_{sp2}$ ,  $r_{sd1}$ , and  $r_{sd2}$  indicate the radii of circular shapes of the lower and upper parts of the center ligament route of MCP pitch, PIP, and DIP joints, respectively.

Please note that the coupling wires with fixed length (orange curves in Fig. 4(c)) are attached at the dorsal side of the distal circular parts and the volar side of the proximal circular parts. This means that the joints can resist shear force produced by pinching with the fingertip. The extension spring is placed in the palm frame. As shown in Fig. 4 (d), the implemented link structure properly adapts to hyperextension, off-axis bending and twisting, and returns to the original pose without damage. However, the excessive force along the joint motion causes excessive tension on the actuation wires and excessive compression to the joint, which cannot be absorbed by the proposed joint mechanism alone and impact absorbing actuators such as SEA, VSJ or highly back-drivable actuators should be used.

### B. Kinematically Accurate Tendon-Driven Mechanism

Hand mechanisms based on soft materials have great advantages when dealing with arbitrarily shaped objects. However, they are susceptible to inaccuracy and their modeling is difficult because of deformation by external and internal forces. Thus,

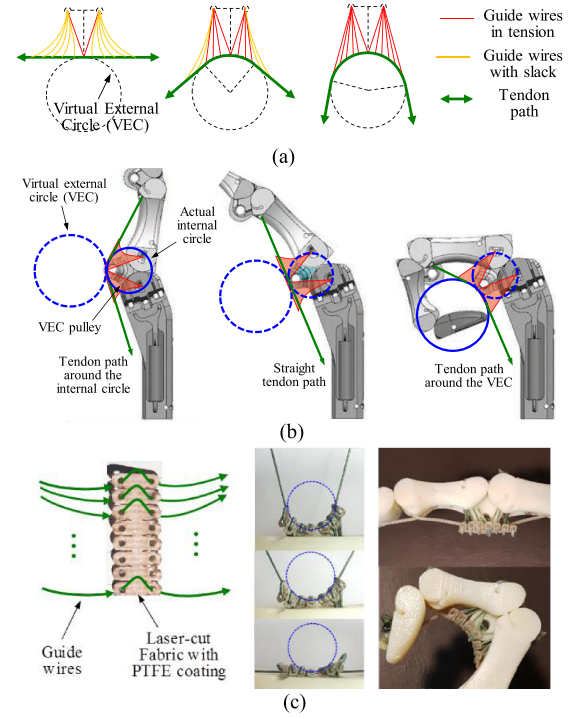


Fig. 5. Virtual external circle (VEC) pulley. (a) Basic concept of the VEC pulley. (b) MCP wire path guided by the VEC pulley and the volar frame. (c) Structure and implementation of the VEC pulley.

an accurate kinematic model is hard to achieve. By contrast, human tendons and pulleys have much higher stiffness than those of soft materials like silicone and urethane. For instance, the measured stiffness of the A2 pulley of the middle finger is 129.59 N/mm [9].

To obtain an accurate kinematic model, a novel soft pulley structure, named virtual external circle (VEC) pulley, was devised. Fig. 5(a) illustrates the basic concept of the VEC pulley. The tendon path is guided by multiple guide wires whose lengths are properly determined (thin yellow and red lines). When the tendon is at a straight pose, as shown in the left figure in Fig. 5(a), most of the guide wires are loosened and do not affect the tendon path. When the tendon becomes bent (the center and right figures of Fig. 5(a)), tension gradually builds up in the guide wires to form the circular tendon path. If the guide wires have sufficient flexibility and high tensile stiffness, the VEC pulley will have consistent circular shape regardless of the change of the tendon tension. This property is helpful for exact kinematic modeling.

Fig. 5(b) shows the VEC pulley applied to the MCP joint. When the MCP joint is fully extended (left figure), the MCP wire goes around the circular groove (actual internal circle) on the MCP volar frame. The figure at the center shows the pose in which the MCP wire becomes straight. If the MCP joint flexes more, as shown in the right figure, the MCP wire goes around the virtual circle formed by the VEC pulley. Therefore, the MCP wire is constrained by the two circles with fixed radii. Similarly, all the actuation wire paths can be represented by lines and arcs with constant radii. Detailed modeling is described in Section IV. Fig. 5(c) shows the implemented VEC pulleys. Braided Dyneema wires were used for the guide wires and laser-cut fabric with PTFE coating was used to maintain the gaps between the guide wires. A wire sliding on a surface with an exceedingly small radius is severely affected by internal stress in

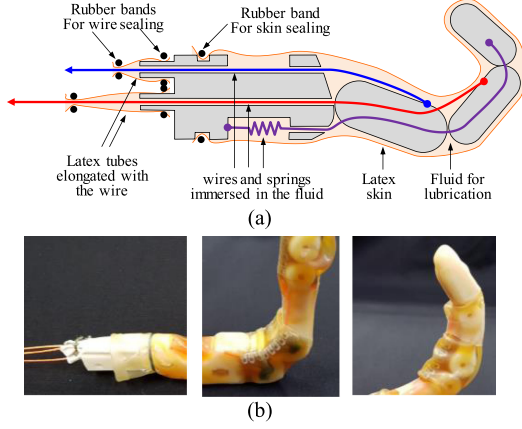


Fig. 6. Latex skins and tubes for the fluid lubrication. (a) Simplified section view of the sealing structure. (b) Detailed view of the skin with lubricant.

the wire, thus it has a short lifetime. However, by utilizing VEC pulleys, the actuation wires can have simple and smooth paths with large bending radii, which is essential to increase efficiency and lifetime.

### C. Skin for Fluid Lubrication

Even though the wire paths were carefully designed for low friction, the proposed mechanism has several points of contact that can cause friction: the contact between the VEC pulley and the actuation wires, and the contact between the center ligament and the frames. To lubricate all these parts, similar to the operation of the synovial fluid, the whole mechanism is surrounded by a latex skin and tubes. Fig. 6(a) illustrates the simplified sealing structure. The finger mechanism, including the finger and volar frames, VEC pulleys, the center ligament, and the extension spring, are covered by a 0.3 mm thickness Latex membrane. The entrance of the membrane is sealed by a band. The three actuation wires are also sealed by latex tubes; both ends of each tube are tightened by bands at the inlets of the palm frame and at the wire. As the latex tubes elongate and shrink with movement of the actuation wires, the whole mechanism can securely contain the lubricating fluid. Fig. 6(b) shows the finger mechanism sealed with the latex skin. SuperGliss 220 K of Motorex Co., which is suitable to reduce stick-slip between engineering plastics, was used as the lubricating fluid.

## IV. KINEMATICS AND STATICS

### A. Kinematics and Jacobian

Fig. 7(a) illustrates the kinematic structure of the finger. As explained in Section III.A and Fig. 4(c), the radii of the two rolling contact surfaces of each joint were determined to have the same values;  $r_m$ ,  $r_p$ , and  $r_d$  for the MCP pitch, PIP, and DIP joints, respectively. The rolling contact surface of the MCP roll joint also has the same radius  $r_a$ . The lengths of the MCP roll, proximal, middle, and distal phalanges are  $l_a$ ,  $l_p$ ,  $l_m$ , and  $l_d$ , respectively. Considering the rolling joints, the finger can be regarded as a serial manipulator with nine links including the base link. Fig. 7(b) shows the coordinate frames at a certain flexed pose. From the proximal end the coordinate frames are defined as  $\Sigma_b$  (base frame),  $\Sigma_{br}$  (a virtual link for the MCP roll joint),  $\Sigma_a$  (MCP roll frame),  $\Sigma_{ar}$  (a virtual link for the MCP pitch joint),  $\Sigma_p$  (proximal link),  $\Sigma_{pr}$  (a virtual link for the PIP joint),

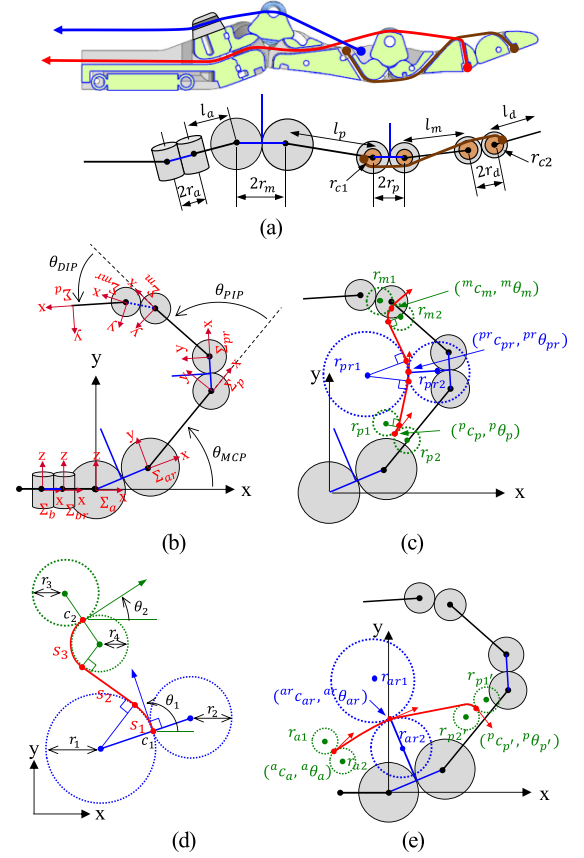


Fig. 7. (a) Kinematic structure of the finger. (b) Joint angles and coordinate frames. (c) Arcs and segments of lines defining the PIP actuation wire. (d) Basic curve constituting the wire paths. (e) Arcs and segments of lines defining the MCP actuation wire.

$\Sigma_m$  (middle link),  $\Sigma_{mr}$  (a virtual link for the DIP joint), and  $\Sigma_d$  (distal link for the fingertip), respectively. The joint angles of the MCP roll, MCP pitch, PIP, and DIP joints are defined as  $\theta_{ROLL}$ ,  $\theta_{MCP}$ ,  $\theta_{PIP}$ , and  $\theta_{DIP}$ , respectively. As illustrated with the brown colored curves in Fig. 7(a), the  $\theta_{PIP}$  and  $\theta_{DIP}$  joints are coupled such that:

$$\theta_{DIP} = \alpha \theta_{PIP} \quad (6)$$

where the ratio  $\alpha$  is set to 2/3 by properly determining the radii of the coupling circles  $r_{c1}$  and  $r_{c2}$ . From (2), the flexion angles of the virtual links between the rolling surfaces are half of the joint angles. For instance, the angle between the x-axes of  $\Sigma_a$  and  $\Sigma_{ar}$  is simply  $\theta_{MCP}/2$ .

If we define the homogenous transform (HT) matrices between the adjacent coordinate frames, arbitrary points in any coordinate frame can be represented with respect to other frames. For instance, the HT matrix from  $\Sigma_p$  to  $\Sigma_{pr}$  is denoted by  ${}^pT_{pr}$ , where the left superscript and right subscript mean the reference frame and the target frame, respectively. The fingertip position  $(x_t, y_t, z_t)$  with respect to  $\Sigma_b$  is obtained as follows:

$$\begin{bmatrix} x_t \\ y_t \\ z_t \\ 1 \end{bmatrix} = {}^bT_{br} {}^{br}T_a {}^aT_{ar} {}^{ar}T_p {}^pT_{pr} {}^{pr}T_m {}^mT_{mr} {}^{mr}T_d \begin{bmatrix} 0 \\ 0 \\ 0 \\ 1 \end{bmatrix} \quad (7)$$

Hereafter, the relationship between the actuation wire lengths and the flexion angles is derived. Fig. 7(c) illustrates the PIP

wire path at the flexion angle  $\theta_{PIP}$ . The path is determined by six circles; two of these are the external and internal circles determined by the VEC pulley and the volar frame (blue dotted circles) and the other four circles are defined by the rounded frame shapes of the insertion point of the distal end of the wire and the tunnel entrance to the proximal frame (green dotted circles). These three pairs of circles are defined by the center positions, tangential angles, and the radii of the left and right adjacent circles;  $(^p c_p, ^p \theta_p, r_{p1}, r_{p2})$ ,  $(^{pr} c_{pr}, ^{pr} \theta_{pr}, r_{pr1}, r_{pr2})$ , and  $(^m c_m, ^m \theta_m, r_{m1}, r_{m2})$  as indicated in Fig. 7(c), where the first and second components of each denote the center position and the tangential angle, and the other two components denote the radii of the two adjacent circles. The left superscripts of the first and second elements represent the coordinated frame where the position and angle are presented. This means that all of these are constant design parameters. As noticed in Fig. 7(c), the path of the PIP wire is composed of multiple arcs and segments like Dubins Curves. In the general case, a path defined by the two pairs of circles  $(c_1, \theta_1, r_1, r_2)$  and  $(c_2, \theta_2, r_3, r_4)$  can be considered as shown in Fig. 7(d). Here, the path length can be calculated by adding the lengths of the two arcs and one segment of the line  $s_1$ ,  $s_2$  and  $s_3$  as

$$l_{path}(c_1, c_2, \theta_1, \theta_2, r_1, r_2, r_3, r_4) = r_4 (\theta_t - \theta_2) + \sqrt{l_{14}^2 - (r_1 + r_4)^2} + r_1 (\theta_t - \theta_1), \quad (8)$$

with  $\theta_t = \theta_{14} + \frac{\pi}{2} - \arccos \frac{r_1 + r_4}{l_{14}}$

where  $\theta_{14}$  and  $l_{14}$  denote the angle and the length of the vector from the center of the circle of  $r_1$  to the center of the circle of  $r_4$ . (8) describes the length of the path for one case among a total of 4 cases: the paths go from the circle of  $r_1$  to that of  $r_3$ , from that of  $r_1$  to that of  $r_4$ , from that of  $r_2$  to that of  $r_3$ , and from that of  $r_2$  to that of  $r_4$ . As the length of the other cases can be calculated in a similar way, let us assume that the function  $l_{path}(c_1, c_2, \theta_1, \theta_2, r_1, r_2, r_3, r_4)$  provides the length of shortest feasible path among them. The path of the PIP wire shown in Fig. 7(c) is the combination of the two curves represented by the  $l_{path}$  function. Consequently, the length of the PIP wire can be obtained as

$$l_{PIP}(\theta_{PIP}) = l_{path}(^p c_p, ^p c_{pr}, ^p \theta_p, ^p \theta_{pr}, r_{p1}, r_{p2}, r_{pr1}, r_{pr2}) + l_{path}(^{pr} c_{pr}, ^{pr} c_m, ^{pr} \theta_{pr}, ^{pr} \theta_m, r_{pr1}, r_{pr2}, r_{m1}, r_{m2}) \quad (9)$$

where  $^p c_{pr}$  and  $^p \theta_{pr}$  are the center point and the tangent angle represented with respect to  $\Sigma_p$  not  $\Sigma_{pr}$ . It means that these are not constant values anymore and the functions of the joint angle  $\theta_{PIP}$ .  $^{pr} c_m$ , and  $^{pr} \theta_m$  are also a function of  $\theta_{PIP}$ . Similarly, as illustrated in Fig. 7(e), the relationship between  $\theta_{MCP}$  and the MP wire length  $l_{MCP}$  is obtained as

$$l_{MCP}(\theta_{MCP}) = l_{path}(^a c_a, ^a c_{ar}, ^a \theta_a, ^a \theta_{ar}, r_{a1}, r_{a2}, r_{ar1}, r_{ar2}) + l_{path}(^{ar} c_{ar}, ^{ar} c_{p'}, ^{ar} \theta_{ar}, ^{ar} \theta_{p'}, r_{ar1}, r_{ar2}, r_{p'1}, r_{p'2}) \quad (10)$$

where the path is defined by three pairs of circles  $(^a c_a, ^a \theta_a, r_{a1}, r_{a2})$ ,  $(^{ar} c_{ar}, ^{ar} \theta_{ar}, r_{ar1}, r_{ar2})$ , and  $(^p c_{p'}, ^p \theta_{p'}, r_{p'1}, r_{p'2})$ .  $l_{PIP}$  and  $l_{MCP}$  describe the actual wire lengths at the given joint angles  $\theta_{MCP}$  and  $\theta_{PIP}$ . Focusing only on the displacement of the wire, the following equations can be used:

$$\begin{aligned} s_{MCP} &= l_{MCP}(0) - l_{MCP}(\theta_{MCP}), \\ s_{PIP} &= l_{PIP}(0) - l_{PIP}(\theta_{PIP}) \end{aligned} \quad (11)$$

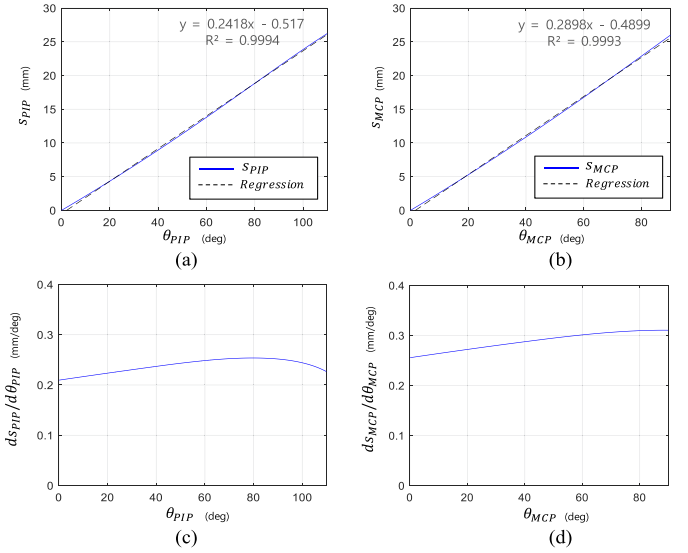


Fig. 8. The relationship between wire displacements and joint angles with linear regression equations.

Fig. 8 shows the graphs of joint angles versus wire displacements obtained by (11). This shows that the proposed mechanism has approximately a linear kinematic property that assures even joint speed and torque with low distortions.

The MCP roll motion is produced by differential motion of the left MCP and right MCP wires. The range of motion is acceptably small compared to the change of wire paths (see Fig. 3(b)), and it can be considered as a linear motion. Therefore, the length of the left and right MCP motions  $s_{lMCP}$  and  $s_{rMCP}$  are:

$$\begin{aligned} s_{lMCP} &= s_{MCP} + \frac{w_{MCP}}{2} \theta_{ROLL}, \\ s_{rMCP} &= s_{MCP} - \frac{w_{MCP}}{2} \theta_{ROLL} \end{aligned} \quad (12)$$

where  $\theta_{ROLL}$  and  $w_{MCP}$  correspond to the MCP roll angle and the distance between the left MCP and right MCP wires. Summarizing the kinematic analysis, (11) and (12) present the inverse kinematics between the wire displacements and the joint angles. Due to the smooth and clear structural properties of the proposed VEC pulley, the mechanism produces an accurate kinematic relationship.

### B. Incremental Kinematics and Statics

By partial differentiation of  $s_{lMCP}$ ,  $s_{rMCP}$ , and  $s_{PIP}$  with respect to  $\theta_{ROLL}$ ,  $\theta_{MCP}$ , and  $\theta_{PIP}$ , the Jacobian matrix  $A$  relating the wire linear speeds and joint angular speeds can be defined as follows:

$$\dot{s} = A \dot{\theta} \quad (13)$$

where  $\dot{s} = [\dot{s}_{lMCP}, \dot{s}_{rMCP}, \dot{s}_{PIP}]^T$  is the vector of the actuation wire speeds and  $\dot{\theta} = [\dot{\theta}_{ROLL}, \dot{\theta}_{MCP}, \dot{\theta}_{PIP}]^T$  is that of the joint speeds. Another Jacobian between the joint angular speeds and the fingertip translational speed can be obtained by differentiating (7) as follows:

$$\dot{x} = J \dot{\theta} \quad (14)$$

where  $\dot{x} = [\dot{x}_d, \dot{y}_d, \dot{z}_d]^T$  is the translational velocity vector of the fingertip. By using the transposes of the Jacobian  $A$ , the relationship between the wire tension and the joint torque can



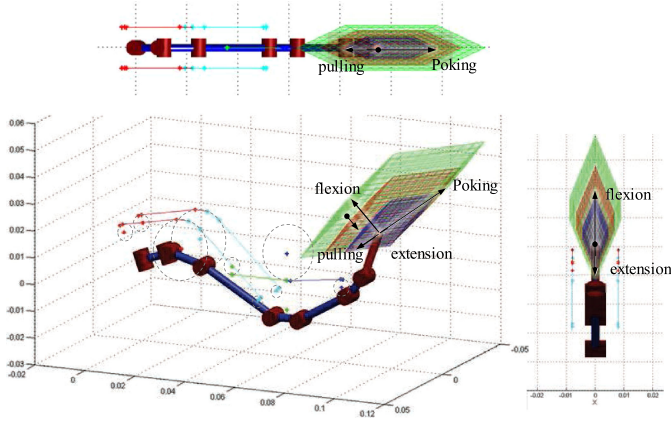


Fig. 9 Simulated finger mechanism with the regions of available fingertip forces; the green, red, and blue regions indicate the force vectors caused by the maximum tensions of 10, 15, and 20 N.

be obtained as follows:

$$\tau = A^T \xi - \tau_{cl} \quad (15)$$

where  $\xi = [\xi_{LMCP}, \xi_{RMCP}, \xi_{PIP}]^T$  is the tension vector of the actuation wires, and  $\tau_{cl} = [0, \tau_{MCP}, \tau_{PIP}]^T$  is the extension torques produced by the extension spring and center ligament. The first component of  $\tau_{cl}$  is zero because the extension torque for the MCP roll joint is not needed. In addition, the relationship between fingertip force  $f$  and joint torque  $\tau$  is

$$f = J^{-T} \tau \quad (16)$$

From (15) and (16), we can calculate the fingertip force for given actuation wire tensions as follows:

$$f = J^{-T} (A^T \xi - \tau_{cl}) \quad (17)$$

For simplicity in the mechanism, the FLLEX finger employs the actuation wires only for the flexion motions, and the center ligament provides passive extension torque. Thus, the finger can exert a limited amount of force in the extension direction. Fig. 9 shows the simulated finger mechanism with the regions of available fingertip forces resulting from several maximum wire tensions. The blue, red, and green polygonal regions show the available fingertip force vectors calculated by (17) with the maximum tensions of 10, 15, and 20 N, respectively. The fingertip force in the flexion direction increases as the wire tension increases, but the force in the extension direction is limited regardless of the wire tension. This is because the extension torque is produced only by the center ligament and extension spring, as in (5). The forces in the poking and pulling directions are also limited. If we increase the force of the extension spring, the fingertip can exert higher flexion force. However, high extension torque also increases undesirable friction and loss of the actuator force. Therefore, the selection of a proper spring is important.

## V. IMPLEMENTATION AND EXPERIMENTAL VALIDATION

The rigid frames are made from 3-D printed material using uPrint SE (Stratasys Co., resolution 0.254 mm). Braided Dyneema wires of LIROS Co. (diameter 1 mm, breaking strength 1910 N) were used for the actuation wires. For the VEC pulleys guide wires, 0.3 mm diameter Dyneema wires were used.

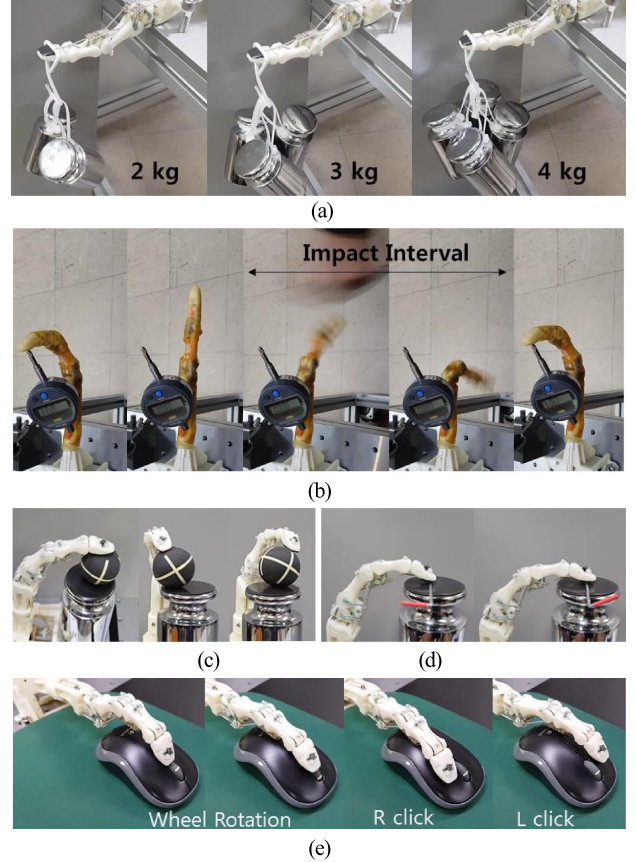


Fig. 10. (a) Force test with 2, 3, and 4 kgf. (b) Impacts during repeatability test, (c) and (d) object manipulation test. (e) Computer mouse manipulation test.

TABLE I  
TEST RESULTS OF REPEATABILITY WITH IMPACTS

No.	distance (mm)	No.	distance (mm)	Average (mm)	1.293
1	1.304	6	1.462	Std. deviation (mm)	0.116
2	1.303	7	1.394		
3	1.233	8	1.248		
4	1.432	9	1.126	Max. deviation (mm)	0.169
5	1.307	10	1.125		

For the wire actuation, 3 Dynamixel-X actuators of ROBOTIS Co. (XM430-W350, stall torque 4.1 Nm) were used. These can produce wire tension of more than 200 N, and the fingertip force in the straight pose was more than 40 N.

Fig. 10(a) shows the experimental results of the force test. The fingertip was set to move 40 mm upward and downward. Weights of 2, 3, and 4 kg were suspended at the fingertip and it was confirmed that the finger moved without failure or damage. To verify the robustness and precision of the proposed mechanism, a repeatability test during impact was conducted. Fig. 10(b) shows snapshots of the experiment. Ten measurements of the fingertip position were performed using a dial gauge (Mitutoyo Co. resolution 0.001 mm). During the intervals between the measurements, impacts causing hyperextensions and twists were applied nine times. As the actuators do not have sufficient back-drivability and sufficiently low inertia, the actuation wires were set to slack during the impacts. As shown in Table I, the standard deviation and maximum deviation from the average distance

TABLE II  
100 ITERATIONS OF REPEATABILITY TEST WITHOUT IMPACTS

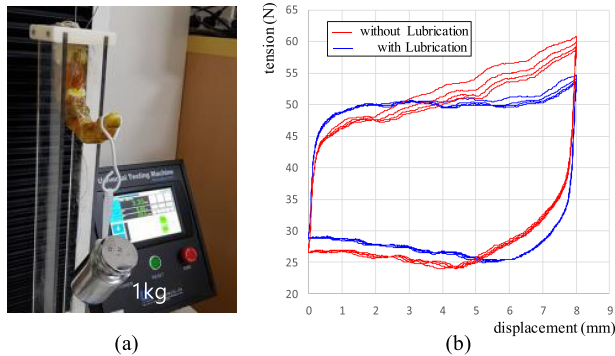
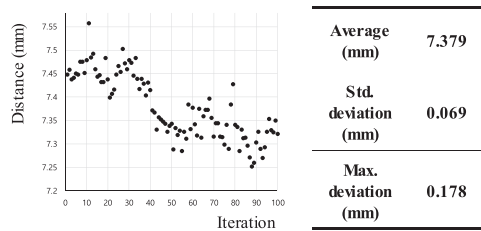


Fig. 11. (a) Experimental setup to assess effect of the fluid lubrication. (b) measured tension and displacement relationship of the PIP wire (red: without lubrication, blue: with lubrication).

were 0.166 mm and 0.169 mm, respectively, which were notably small values for a tendon-driven mechanism. For thorough repeatability verification, 100 iterations of similar experiments without impacts were performed. The results are summarized in Table II, where standard deviation and maximum deviation from the average distance were 0.069 mm and 0.178 mm, respectively. These results prove the robustness and precision of the proposed center ligament structure and the fluid lubricated mechanism using VEC pulleys.

To assess the effect of fluid lubrication, the tension according to the wire displacement was measured. Fig. 11(a) shows the experimental setup. A universal test machine (WL2100, Withlab Co. Max force 100 kgf) was used to measure the tension of the PIP wire. Taking one of the worst cases, the MCP joint was maintained at the fully bent angle 90 deg, and 1 kg load was applied at the fingertip. The PIP actuation wire was pulled by 8 mm with the speed of 20 mm/min. The red and blue curves in Fig. 11(b) show the displacement and tension relationship without and with the lubricant, where the maximum tensions were 60.8 N and 54.6 N respectively. Even though the efficiently designed wire path and the low friction of the PTFE coated VEC pulley decrease the friction, the lubricant decreases it more. The lubricant is also expected to increase robustness and longevity.

To validate the dexterous manipulation performance, several manipulation tests were conducted. Fig. 10(c) shows snapshots of a ball being manipulated in the pitch and roll directions. Here, the finger mechanism was soaked with lubricating fluid, rather than being covered by the latex skin. Fig. 10(d) shows the task of rolling a 2 mm shaft with a constant speed. This task needs precise fingertip control without stick-slip. The finger performed these two tasks consistently at high speeds as well as low speeds.

To assess the potential advantages in human activities of daily living (ADL) tasks, the manipulation of a computer mouse was tested, as shown in Fig. 10(e). The finger was set to do the wheel rotation, right button click, and left button click. In particular, the wheel rotation requires fingertip motions in the poking and pulling directions, as mentioned in Fig. 9. Because the design parameters and the spring stiffness were properly determined, considering these tasks, the experiment found that the finger has sufficient range of motion, force, and speed to perform the button click and wheel rotation.

## VI. CONCLUSION AND FUTURE WORK

This letter presented a novel 3-DOF finger mechanism, which features impact absorbing performance, high precision, and high force. The advantageous properties of human hands were analyzed, and their fundamental principles were adopted. The proposed center ligament structure, inspired by human joints with collateral ligaments, can absorb undesirable forces. A cable-driven mechanism with unique VEC pulleys allows high fingertip force and accurate kinematic modeling. As the entire moving parts are submerged in lubrication fluid with a latex skin, the finger mechanism has high efficiency and control performance. As future research, a 5-fingered 12-DOF hand with proper fingertip shape and back-drivable actuators with a tension-limiting clutch mechanism will be developed. Developing soft and robust artificial skin appropriate for long-term operation is also an important research topic. The properties of human hands which enable outstanding performance such as the pull-up, handstand, punching, as well as other delicate motions will be considered and adopted in taking the FLLEX hand to full human hand capabilities.

## REFERENCES

- [1] A. D. Deshpande *et al.*, "Mechanisms of the anatomically correct testbed hand," *IEEE/ASME Trans. Mechatronics*, vol. 18, no. 1, pp. 238–250, Feb. 2013.
- [2] Z. Xu and E. Todorov, "Design of a highly biomimetic anthropomorphic robotic hand towards artificial limb regeneration," in *Proc. IEEE Int. Conf. Robot Autom.*, 2014, pp. 2562–2563.
- [3] M. Grebenstein *et al.*, "Antagonistically driven finger design for the anthropomorphic DLR hand Arm system," in *Proc. IEEE Int. Conf. Intell. Robots Syst.*, 2011, pp. 1836–1842.
- [4] Dec. 22, 2012. [Online]. Available: <https://www.shadowrobot.com/products/dexterous-hand/>
- [5] Y.-J. Kim *et al.*, "RoboRay hand: A highly backdrivable robotic hand with sensorless contact force measurements," in *Proc. Int. Conf. Robot. Autom.*, 2014, pp. 6712–6718.
- [6] Cosimo *et al.*, "Toward dexterous manipulation with augmented adaptive synergies: The pisa/IIT soft hand 2," *IEEE Trans. Robot.*, vol. 34, no. 5, pp. 1141–1156, Oct. 2018.
- [7] Aug. 8, 2017 [Online]. Available: <https://robotiq.com/products/3-finger-adaptive-robot-gripper>
- [8] B. K. Jones *et al.*, "The friction coefficient of shoulder joints remains remarkably low over 24 h of loading," *J. Biomechanics*, vol. 48, no. 14, pp. 3945–3949, Nov. 2015.
- [9] G.T. Lin *et al.*, "Mechanical properties of human pulleys," *J. Hand Surgery*, vol. 15B, no. 4, pp. 429–434, Nov. 1990.
- [10] A. Mottard, T. Laliberté, and C. Gosselin, "Underactuated tendon-driven robotic/prosthetic hands: Design issues," in *Proc. Conf. Robot., Sci. Syst.*, Cambridge, Massachusetts, USA, Jul. 2017, doi: 10.15607/RSS.2017.XIII.019.
- [11] G. Bai *et al.*, "Self-adaptive monolithic anthropomorphic finger with teeth-guided compliant cross-four-bar joints for underactuated hands," in *Proc. IEEE-RAS 18th Int. Conf. Humanoids*, Nov. 2018, pp. 145–152.